

Study of solidification cracking in advanced high strength automotive steels

Agarwal, Gautam; Gao, He; Amirthalingam, Murugaiyan; Richardson, Ian; Hermans, Marcel

DOI

[10.3217/978-3-85125-615-4](https://doi.org/10.3217/978-3-85125-615-4)

Publication date

2018

Document Version

Final published version

Published in

Mathematical Modelling of Weld Phenomena 12

Citation (APA)

Agarwal, G., Gao, H., Amirthalingam, M., Richardson, I., & Hermans, M. (2018). Study of solidification cracking in advanced high strength automotive steels. In C. Sommitsch, N. Enzinger, & P. Mayr (Eds.), *Mathematical Modelling of Weld Phenomena 12* (Vol. 12, pp. 465-483). Verlag der Technischen Universität Graz. <https://doi.org/10.3217/978-3-85125-615-4>

Important note

To cite this publication, please use the final published version (if applicable).
Please check the document version above.

Copyright

Other than for strictly personal use, it is not permitted to download, forward or distribute the text or part of it, without the consent of the author(s) and/or copyright holder(s), unless the work is under an open content license such as Creative Commons.

Takedown policy

Please contact us and provide details if you believe this document breaches copyrights.
We will remove access to the work immediately and investigate your claim.

STUDY OF SOLIDIFICATION CRACKING IN ADVANCED HIGH STRENGTH AUTOMOTIVE STEELS

G. AGARWAL*, H. GAO**, M. AMIRTHALINGAM***,
I. M. RICHARDSON* and M. J. M. HERMANS*

*Department of Materials Science and Engineering, Faculty of 3mE, Delft University of Technology, Mekelweg 2, 2628CD Delft, The Netherlands, G.Agarwal@tudelft.nl, I.M.Richardson@tudelft.nl, M.J.M.Hermans@tudelft.nl

**Tata Steel, P.O. Box 10000, 1970 CA IJmuiden, The Netherlands, He.Gao@tatasteelurope.com

***Department of Metallurgical and Materials Engineering, Indian Institute of Technology Madras, Chennai 600036, India, murugaiyan@iitm.ac.in

DOI 10.3217/978-3-85125-615-4-25

ABSTRACT

Advanced high-strength steels (AHSS), which are increasingly used in the automotive industry, meet many functional requirements such as high strength and crash resistance. Some of these steels contain high amounts of alloying elements, which are required to achieve the necessary mechanical properties, but render these steels susceptible to weld solidification cracking. Weld solidification cracking results from the complex interplay between mechanical and metallurgical factors. Our recent work is focused on studying solidification cracking in dual phase (DP) and transformation induced plasticity (TRIP) steels using the following modeling and experimental strategies:

1. A finite element (FE) based model was constructed to simulate the dynamic thermal and mechanical conditions that prevail during bead-on-plate laser welding. To vary the restraint, laser welding was carried out on single sided clamped specimens at increasing distances from the free edge. In TRIP steel sheets, solidification cracking was observed when welding was carried out close to the free edge and at a certain minimum distance, no cracking was observed. For the no cracking condition, *in situ* strain evolution during laser welding was measured by means of digital image correlation to validate the strain from the FE-model. Subsequently, a phase field model was constructed using the validated thermal cycles from the FE-model to simulate the microstructural evolution at the tail of a weld pool, where primary dendrites coalesce at the weld centerline. From the phase field model, elemental segregation and stress concentration are used to explain the cracking susceptibility in TRIP and DP steels. For DP steel, both the experimental and modeling results indicate a higher resistance to solidification cracking.

2. A phase field model was constructed to simulate the directional solidification in TRIP and DP steels. The thermal cycle and temperature gradient were derived from the *in-situ* solidification experiments conducted using high temperature laser scanning confocal microscopy (HTLSCM). The model showed that longer and narrower interdendritic liquid channels exist in the case of TRIP steel. For the TRIP steel, both the phase field model and atom probe tomography revealed notable enrichment of phosphorus, which leads to a severe undercooling in the interdendritic region. In the presence of tensile stress, an opening at the interdendritic region is difficult to fill with the remaining liquid due to low permeability, resulting in solidification cracking.

The overall study shows that a combination of factors is responsible for the susceptibility of a material to solidification cracking. These include particularly mechanical restraint, solidification temperature range, solidification morphology, solute segregation and liquid feeding capability.

Keywords: Solidification Cracking, Hot Cracking, Steel, Laser Welding, Automotive, Advanced high strength steels (AHSS)

INTRODUCTION

The CO₂ emission regulation of passenger vehicles has become stringent in the last two decades and the target emission between 2020-2025 seems to converge globally [1] as can be seen in figure 1. One of the fundamental ways to achieve this target in the automotive industry is to reduce the overall weight of the vehicle. Naturally, reduction of weight should not compromise the vehicle performance and passenger safety. To meet this demand, new steels under the umbrella, Advanced High Strength Steels (AHSS) are being increasingly developed and put into use. These steels comprise on an average, 30-35 % of a typical car body (body in white) weight [2] and possess high strength, ductility and toughness. The increased strength and ductility allows the use of thinner gauge steels thus reducing the vehicle weight. AHSS are used in chassis components, B-pillars, crash boxes, engine cradles etc. [3].

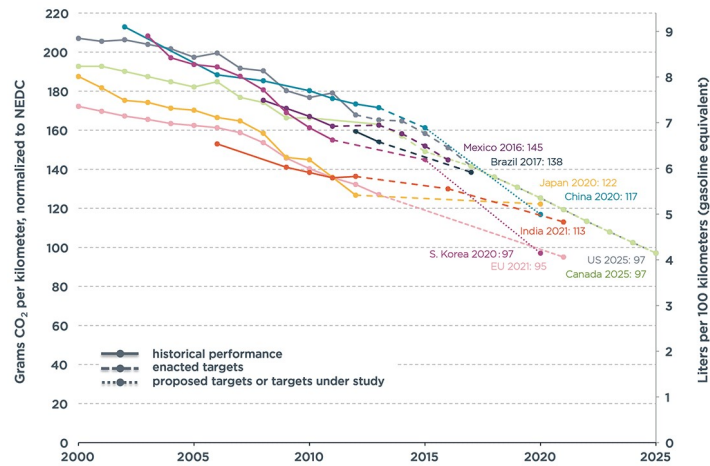


Fig. 1 Passenger car CO₂ emission standard and fuel consumption, normalized to New European Driving Cycle (NEDC). The figure also indicates the proposed emission standard of various countries [1].

Apart from formability requirements in these steels, weldability of such steels is an important aspect. The higher content of alloying elements in some of the AHSS, required for achieving necessary mechanical properties, render them susceptible to solidification cracking during welding. Solidification cracking, also known as hot tearing or hot cracking in casting, occurs due to a complex interplay between mechanical and metallurgical conditions, that are generated during the weld thermal cycle. During weld metal solidification, columnar grains grow perpendicular to the fusion boundary since the temperature gradient here is at its steepest and accordingly the heat extraction is maximised. The solidifying dendrites meet at the weld centreline. The solidifying weld metal shrinks due to solidification shrinkage and thermal contraction. As solidification progresses, the

solid in the mushy zone begins to form a rigid network, *i.e.*, tensile strain is induced. If the deformation exceeds a certain threshold, separation of the dendrites at the grain boundary can occur. At the terminal stage of solidification, such an opening cannot be compensated by the remaining liquid due to both low permeability and high solid fraction [3–4]. As a result, solidification cracking occurs. Eskin *et al.* [6] in their review paper, elaborated existing hot tearing theories and models. These models are based on the existence of a critical stress, critical strain or critical strain rate criterion that leads to cracking. Katgerman [7] in his mathematical model considered stresses and insufficient feeding in the vulnerable temperature range to be the cause of hot cracking. Recent physical models from Rappaz *et al.* [8] and Kou [9] indicate that in the presence of local deformation, insufficient liquid feeding in the interdendritic or intergranular region results in cracking. Experiments by Coniglio *et al.* [10] also indicate that the presence of a critical strain rate is responsible for cracking. The mechanism of solidification cracking is still not properly understood [11], particularly experiments or models focussing on determining the physical mechanism leading to the separation of grains are lacking.

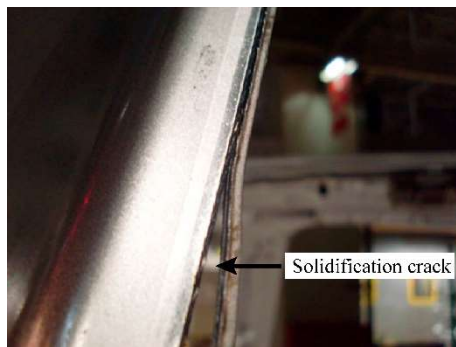


Fig. 2 Solidification cracking in the B-pillar of a Volvo XC60 car body. With permission from [12].

In the assembly lines of car bodies, preformed parts are welded in a flange geometry and the width of the flange is reduced to decrease the weight of the car body. As reported by Omar [14], a typical car body has 40 m of weld flanges that are welded using resistance spot welding. Resistance spot welding requires 16 mm of flange width to fit the electrode system on either side [15]. The flange width can be minimised by using laser welding and can lead to an overall weight reduction of up to 30–40 kg [14]. However, below a critical distance from the flange edge, solidification cracking is often reported. For instance, it is reported [12] that solidification cracking can occur during laser welding of the B-pillar used in Volvo XC60 (figure 2). In order to test the resistance to solidification cracking in thin sheets, VDEh (German Steel Institute) has developed a self-restraint hot cracking test [13]. In this test, bead-on-plate laser welding is conducted on single sided clamped rectangular steel sheets. The starting position is set at a distance of 3 mm from the free edge with the welding direction inclined 7° to the edge. Crack length is used to assess the hot cracking susceptibility of various alloys. The test is of practical importance for overlap and flange welding geometries in order to minimise the flange width.

In the present work, solidification cracking was studied in two commercial automotive AHSS, *i.e.*, transformation induced plasticity (TRIP) and dual phase (DP) steels. These

steels are extensively used in automotive car bodies [16] and hence make a good case for the present study. The following two approaches were implemented:

- Laser bead-on-plate welding experiments were carried out on single sided clamped rectangular sheets, similar to the VDEh standard test. However, the welding direction was kept parallel to the free edge. In TRIP steel, solidification cracking was observed when welding was carried out close to the free edge and beyond a certain distance from the free edge, solidification cracking was not observed. A 3D finite-element (FE) sequential thermal-mechanical model of the laser welding was created. The thermal model was validated by the experiments using both the temperature measurements and weld bead size. The mechanical model was further validated using the experimentally measured transverse strain by the digital image correlation (DIC) technique [17]. Subsequently, a phase field model for solidification under laser welding conditions was created for both TRIP and DP steels. The boundary conditions were adopted from the FE-model. A pre-described global strain of 0.1 % magnitude was applied perpendicular to the weld centreline. The focus was on the solidification behaviour at the weld centreline behind the weld pool and particularly on the conditions that lead to the separation of grains. The approach is described schematically in figure 3.
- A phase field model was created to simulate the directional solidification in both steels using the thermal conditions from the experiments. In-situ solidification experiments were conducted using a high temperature laser scanning confocal microscope. A circular melt pool was formed at the centre of thin disks while the outer rim remained solid in order to provide the restraint. Solidification cracking was observed in the case of TRIP steel while the DP steel was observed to be resistant to solidification cracking.

The results are discussed pertaining to the effect of the solidification temperature range, the interdendritic segregation of phosphorus, liquid feeding tendency, dendrite coherency and the surrounding restraint on the solidification cracking susceptibility.

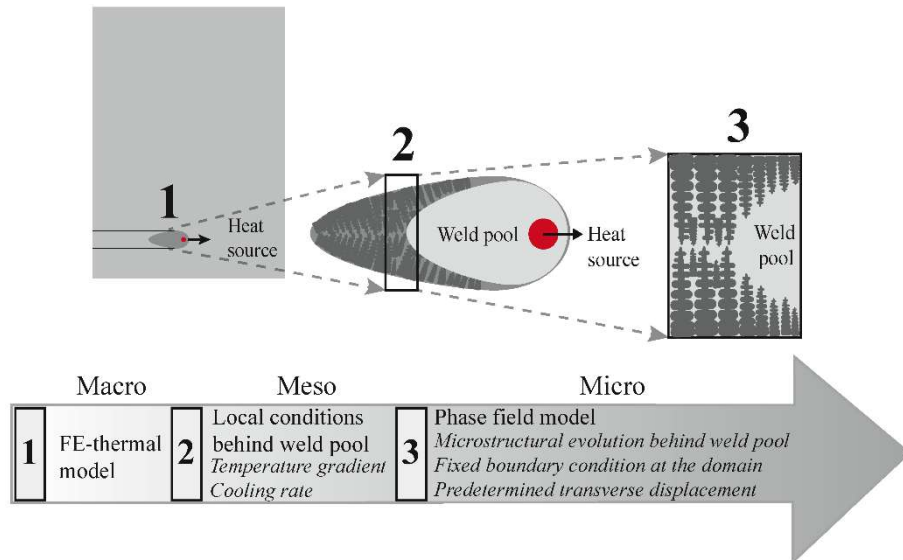


Fig. 3 Schematic of the approach adopted in the present work. At first, a FE-thermal model of laser welding was created. The local thermal gradient behind the weld pool (from the FE-thermal model) along with the thermodynamic and mobility data from Thermo-Calc™ were used in the phase field model of solidification.

EXPERIMENTAL SETUP

The composition of the steels used in this work is listed in Table 1. The experimental arrangement for the laser welding experiments is shown in figure 4. Laser bead-on-plate welding experiments were conducted using a 3 kW Nd:YAG laser in the keyhole mode. Specimens were kept at the focal point of the optical system and the laser spot size was 0.6 mm. A laser power of 1100 W and a welding speed of 10 mm s⁻¹ were used. Rectangular steel sheets with dimensions of 90 × 45 mm² and thickness of 1.25 mm were used. The starting position of the laser (Y ordinate) was varied from 5 mm to 13 mm with each increment being 2 mm. Each experiment was repeated five times. For the 13 mm case, temperature was measured at three locations (figure 4) using spot welded K-type thermocouples. Also, the displacement field during welding was measured using the digital image correlation (DIC) method. More details on the method can be found in our previous work [16–17].

The weld surface and cross section were prepared for optical microscopy using standard procedures. Etching was carried out using 4 % Picral and 2 % aqueous sodium metabisulfite [19]. The fracture surface was observed using a scanning electron microscope.

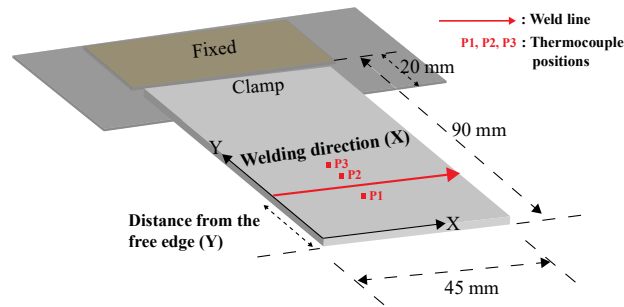


Fig. 4 Schematic of the hot cracking test setup. The thermocouple positions are also indicated. P1 is 3 mm from the weld centreline (towards the free edge) and P2, P3 are 3 mm and 4.5 mm from the weld centreline (towards the constrained edge). Adapted from [17].

Table 1 Composition of the steels used in this work.

Elements, wt.%	C	Mn	Al	Si	Cr	P	Fe
TRIP	0.19	1.63	1.1	0.35	0.019	0.089	bal.
DP	0.15	2.3	0.03	0.10	0.56	0.01	bal.

In-situ solidification experiments were conducted using high temperature laser scanning confocal microscopy. Circular disk-shaped specimens with a diameter 10 mm and a thickness 250 μm were prepared. The sample was placed in an alumina crucible and was held by ceramic protrusions at the periphery of the crucible. The crucible was held in a platinum holder with a thermocouple spot-welded to it. The sample was placed at the upper focal point of a gold-plated ellipsoidal cavity and was heated by radiation using a 1.5 kW halogen lamp placed at the lower focal point. An inert atmosphere was maintained using high purity argon gas. A stable melt pool with a diameter of 3-3.5 mm was formed at the centre of the specimen while the outer rim remained solid. A cooling rate of 10 K s^{-1} was applied until 1623 K using a PID controller, which controls the lamp power appropriately. The temperature at the platinum holder was recorded and concurrently images were acquired at a rate of 30 frames per second. More information on the technique and the setup can be found in references [3], [19–22].

FINITE-ELEMENT (FE) MODEL

A 3D finite element (FE) sequential thermal mechanical model for the welding process was created using a commercial software, COMSOLTM. The heat balance during welding was simulated including the heat input, heat transfer and heat loss. A 3D conical Gaussian heat source as used by [24]–[26] was adopted to describe the laser beam heat input. The thermal history, *i.e.*, temperatures (T) at (x, y, z) were obtained by solving the following Fourier heat transfer equation using the temperature-dependent thermal properties of the material,

$$\frac{\partial}{\partial x}\left(k(T)\frac{\partial T}{\partial x}\right) + \frac{\partial}{\partial y}\left(k(T)\frac{\partial T}{\partial y}\right) + \frac{\partial}{\partial z}\left(k(T)\frac{\partial T}{\partial z}\right) + Q_v = \rho(T)C_p(T)\left(\frac{\partial T}{\partial t}\right) \quad (1)$$

Here, $k(T)$ is the temperature dependent thermal conductivity, Q_v is the net volumetric heat flux from the heat source, $\rho(T)$ is the temperature dependent density and $C_p(T)$ is the temperature dependent specific heat.

The temperature dependent thermal and mechanical properties of the steel used in the present work were taken from the reference [18]. Latent heat, absorbed or released during melting (or solidification) is incorporated in the temperature dependent specific heat capacity. The latent heat absorbed during melting was related to the temperature-phase fraction data, obtained using Scheil-Gulliver solidification approximation. The thermal expansion coefficient during solidification is considered to be dependent on the amount of solid and liquid phases. The solidification temperature range, solid and liquid phase fraction data of the steel composition were obtained from a commercial thermodynamic software, Thermo-CalcTM. Quadratic elements with a minimum mesh size of $0.3 \times 0.3 \text{ mm}^2$ and a thickness of 1 mm were used. The process efficiency of laser welding was assumed to be 40 % based on previous work of [27] on the same experimental arrangement. It is thus assumed that the heat losses due to convection and radiation in the keyhole are taken into account.

PHASE-FIELD (PF) MODEL

The phase field modelling approach applied in this study is based on our recent work [23], [28]. Figure 3 shows schematic of the methodology adopted in this work. The emphasis was on the microstructural evolution during solidification at the tail of the weld pool. For this, the local conditions like transient temperature profiles and thermal gradient were taken from the FE-model of laser welding. A commercial software, MICRESSTM based on the phase field approach for multiphase systems was employed. It utilises the thermodynamic (TCFE6) and mobility database (MOB2) from Thermo-CalcTM. A two dimensional grid of $200 \times 300 \text{ }\mu\text{m}$ with a grid size of $1 \text{ }\mu\text{m}$ was defined. The energy parameters for the phase interaction used in this simulation were taken from reference [29] and are listed in table 2. The initial concentration of the components was set to be the bulk composition in the liquid phase. One nucleus of δ -ferrite was placed at the bottom and the top left corner of the computational domain. The radius of the nucleus was set to $0.5 \text{ }\mu\text{m}$. During solidification, the system underwent a liquid to solid reaction based on the local thermodynamic and chemical conditions. Only the cooling cycle behind the weld pool was considered.

For the thermal conditions, transient temperature profiles at the fusion boundaries from the FE model were applied to both edges of the domain. A thermal gradient was defined according to the temperature difference from the fusion to the weld centre line. The initial temperature at the bottom edge was given as the liquidus temperature. The boundary conditions for the phase and concentration were set to be symmetrical. The interface thickness was assumed to be $3 \text{ }\mu\text{m}$. The time evolution is calculated by a set of phase field equations deduced by the minimization of the free energy functional,

Table 2 Energy parameters for liquid to δ -ferrite phase interaction.

Surface energy	$1.6 \times 10^{-1} \text{ J/m}^2$
Kinetic coefficient	$7.3 \times 10^{-11} \text{ m}^4/(\text{J s})$
Static anisotropy coefficient	0.45
Kinetic anisotropy coefficient	0.3

$$\dot{\phi}_\alpha = \sum_\beta M_{\alpha\beta}(\vec{n})(\sigma_{\alpha\beta}^*(\vec{n})K_{\alpha\beta} + \frac{\pi}{\eta}\sqrt{\phi_\alpha\phi_\beta}\Delta G(\vec{c}, T)) \quad (2)$$

$$K_{\alpha\beta} = \phi_\beta \nabla^2 \phi_\alpha - \phi_\alpha \nabla^2 \phi_\beta + \left(\frac{\pi}{\eta}\right)^2 (\phi_\alpha - \phi_\beta) \quad (3)$$

where, ϕ is a phase field parameter, α indicates solid phase, β indicates liquid phase, η is the interface thickness, $M_{\alpha\beta}$ is the mobility of the solid-liquid interface as a function of the interface orientation, described by the normal vector \vec{n} . $\sigma_{\alpha\beta}^*$ is the anisotropic surface stiffness, $K_{\alpha\beta}$ is related to the local curvature of the interface, ΔG is the thermodynamic driving force as a function of temperature T and local chemical composition \vec{c} .

For the stress analysis, a fixed strain of 0.1 %, normal to the welding direction was applied to the phase field domain. A constant elastic modulus of 10 GPa for solid [30] and 1 GPa for liquid [10], [31] was used for both the steels. A thermal expansion coefficient of $2.5 \times 10^{-5} \text{ K}^{-1}$ for the solid phase and $3 \times 10^{-5} \text{ K}^{-1}$ for the liquid phase was employed.

A similar approach was adopted to simulate the directional solidification observed from the *in-situ* solidification experiments. TRIP steel composition, with and without P was considered (referred to as TRIP-No P). Cooling rate and thermal gradient were based on experimental results. Four nuclei of δ -ferrite with an undercooling of 5 K were placed at the underside of the phase field domain. The size of the phase field domain was set to $150 \times 200 \mu\text{m}$ with a grid size of $2 \mu\text{m}$. The stress in the solid phase due to solidification shrinkage and thermal contraction was calculated by fixing the boundaries of the domain. Elastic constant and thermal expansion coefficient of the solid and liquid phases were chosen as described previously.

RESULTS

LASER WELDING EXPERIMENTS

Solidification cracking was observed in the TRIP steel when welding was carried out close to the free edge ($x = 5 \text{ mm}$ from the free edge). With the same welding parameters, the DP steel showed no signs of solidification cracking. Figures 5 (a-b) shows high-speed camera images taken during welding. A solidification crack at the weld centreline was observed to follow the heat source and complete fracture (figure 5 (b)) was observed when welding was carried out close to the free edge. Figure 5 (c) shows an optical macrograph revealing a

weld centreline crack. Figure 5 (d) shows a secondary electron micrograph of the fracture surface with dendritic morphology, a typical feature of solidification cracking [32].

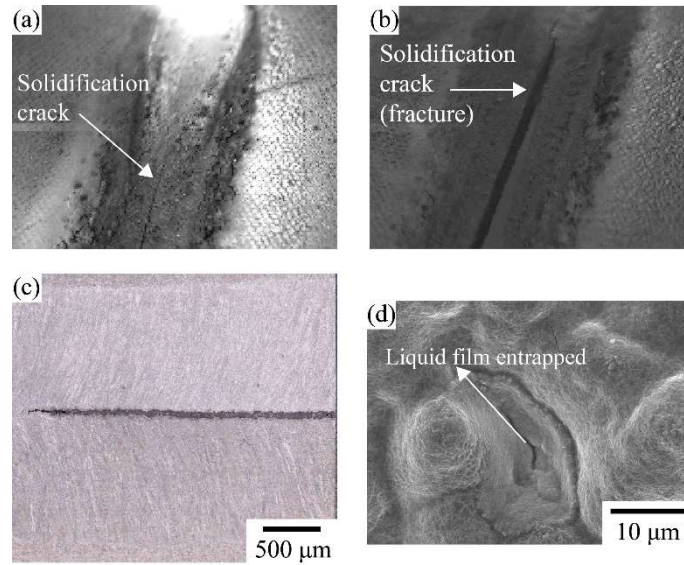


Fig. 5 Laser bead-on-plate welding of TRIP steel sheets. (a) high speed camera image showing solidification crack following the heat source, (b) high speed camera image showing complete fracture, (c) an optical macrograph indicating centerline cracking in TRIP steel, (d) secondary electron micrograph of the fracture surface showing a dendritic morphology. Figures 5 (a) and (c) are taken from reference [23].

To vary the amount of restraint, the starting distance of welding from the free edge was increased. As the distance increased, the average crack length was found to decrease and when welding was carried out at a distance of 13 mm, no solidification cracking was observed. Figure 6 show the experimental and calculated thermal cycle at points P1, P2 and P3 respectively. A good agreement was found between the measured and calculated thermal cycles. Weld bead size was also found to be in good agreement with the thermal model. Subsequently, the temperature gradient and the cooling rate history, behind the weld pool, were extracted from the validated FE-thermal model. The extracted thermal profile was subsequently used in the phase field model.

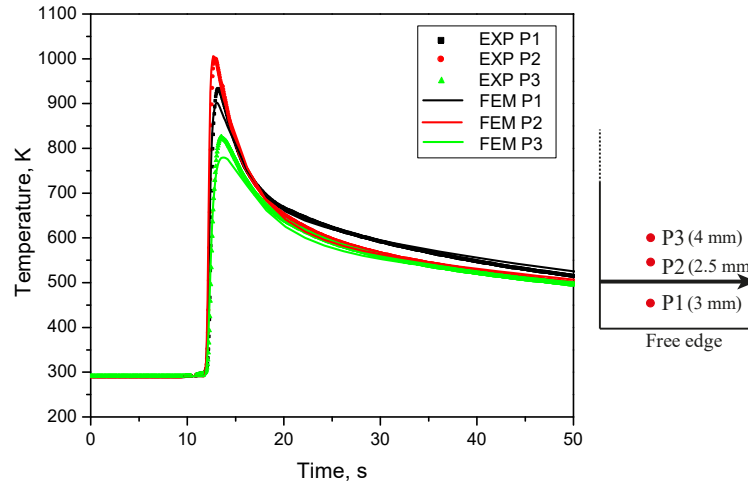


Fig. 6 Experimental and calculated temperature cycles for the 13 mm case. The position of the points P1, P2 and P3 with respect to the weld centreline is also indicated. P1 is at a distance of 3 mm (towards free edge) while P2 and P3 are at 2.5 mm and 4 mm (towards the fixed edge).

IN-SITU SOLIDIFICATION EXPERIMENTS

Figure 7 (a) indicates the diameter of the weld pool achieved before the cooling cycle was started in the in-situ solidification experiment of TRIP steel. Figures 7 (b-f) show the solidification sequence of the TRIP steel. Due to a temperature gradient in the thickness direction, solidification was observed to occur from the underside of the specimen (figure 7 (c)). Solidification cracking was observed during the last stage of solidification (figures 7 (c-d)). Concurrently, isolated liquid droplets were also observed (figure 7 (d)) at low temperatures indicating the presence of strong undercooling. The complete extent of cracking is shown in the secondary electron micrograph taken after the experiment (figure 7 (a)). Under same conditions, solidification cracking was not observed in DP steel [23].

Based on the average solidification rate of the dendrites from the underside to the top, a thermal gradient of 200 K mm^{-1} was applied in the phase field model.

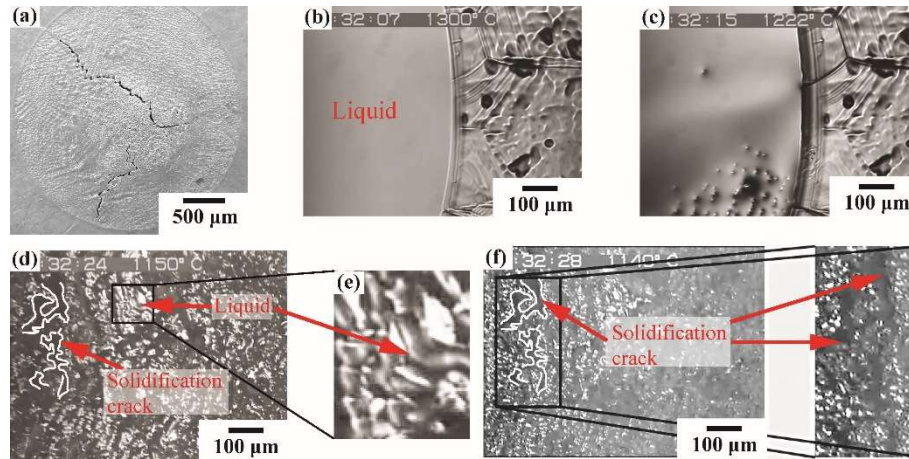


Fig. 7 In-situ solidification experiments (a) secondary electron micrograph showing the extent of solidification cracking, (b-f) solidification images from the confocal microscope, (b) a circular melt pool at the centre of the specimen, (c) dendrites growing mostly from the bottom of the pool, (d-e) solidification crack and isolated liquid pockets, (f) solidification crack observed *in-situ* at the last stage of solidification. Temperature indicated in images (b-d) and (f) is measured at the periphery of the platinum specimen holder. Taken from reference [23].

PHASE FIELD MODELLING

Figures 8 (a) through (d) show the solidification sequence of δ -ferrite columnar dendrites behind the weld pool in TRIP steel. Solidification begins at the fusion boundary with δ -ferrite as the first solid phase (figure 8 (a)). As the heat source (or weld pool) moves further, solidification progresses and columnar dendrites impinge (or coalesce) at the weld centreline (figures 8 (b-c)). Note that due to the restriction of imposing thermal gradient only in the y direction, the direction of solidification is fixed, *i.e.*, perpendicular to the fusion boundary (domain boundary). Figure 8 (e) shows the solidification morphology in DP steel with approximately the same solid fraction as that of TRIP steel in figure 8 (c). The secondary arm dendritic structure is more prominent in TRIP steels. This is also evident from the microsegregation of phosphorous. Figures 8 (f) and (g) shows the P map in TRIP and DP steel. Note the scale difference in P due to nominal compositional difference of P in both the steels. Phosphorous microsegregation of more than two times the nominal composition exists in the case of TRIP steel.

Figure 8 (h) shows the normal stress map in TRIP steel at $t = 0.011$ s. Stress distribution along the arrow as indicated in figure 8 (h) was extracted for both the steels and is shown in figure 9. A more prominent dip in stress at the grain boundaries exist in TRIP steel when compared with DP steel.

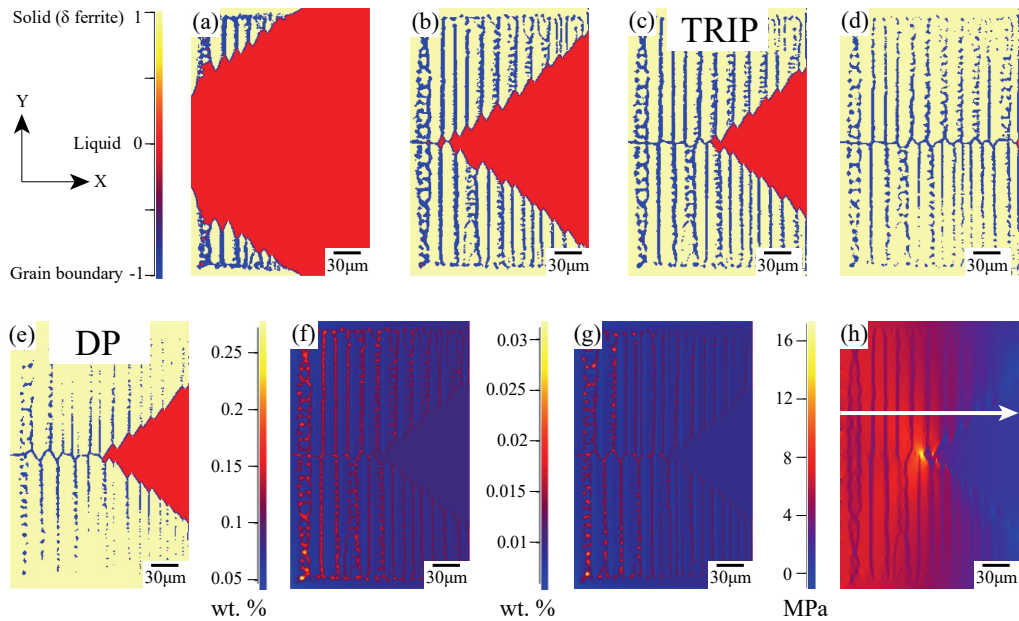


Fig. 8 Phase field simulation of solidification behind the weld pool. (a) solidification starts at the fusion boundaries behind the weld pool in TRIP steel, (b) columnar dendrites of δ -ferrite impinge at the centre at $t=0.011$ s, (c) solidification continues as weld pool progresses further, (d) primary solidification (δ -ferrite) is complete, (e) solidification structure of DP steel at $t=0.01$ s, (f) P map in TRIP steel at $t=0.011$ s, (g) P map in DP steel at $t=0.01$ s, (h) normal stress map in TRIP steel at $t=0.01$ s. An arrow is also marked along which the stress data is extracted for both the steels.

Figures 10 (a) and (b) show the solidification morphology/state in TRIP and TRIP-No P steel respectively. Solidification occurs at a faster rate in TRIP-No P steel, *i.e.*, without P. Also, long and narrow liquid channels exist in TRIP steel with P. Figure 10 (c) shows the P map in TRIP steel, indicating the presence of microsegregation. Microsegregation of P in the interdendritic/intercellular regions leads to undercooling. Figure 11 (a) shows the temperature *versus* solid fraction (f_s) curves of TRIP and TRIP-No P steel based on equilibrium and the present phase field model. The phase field model also indicates the presence of strong undercooling in the interdendritic regions in the TRIP steel, in agreement with the experimental observations. Figures 11 (b) and (c) shows the tensile stress maps for both of the steels. Higher tensile stress (and concentration at the dendrite roots) exists in the TRIP steel.

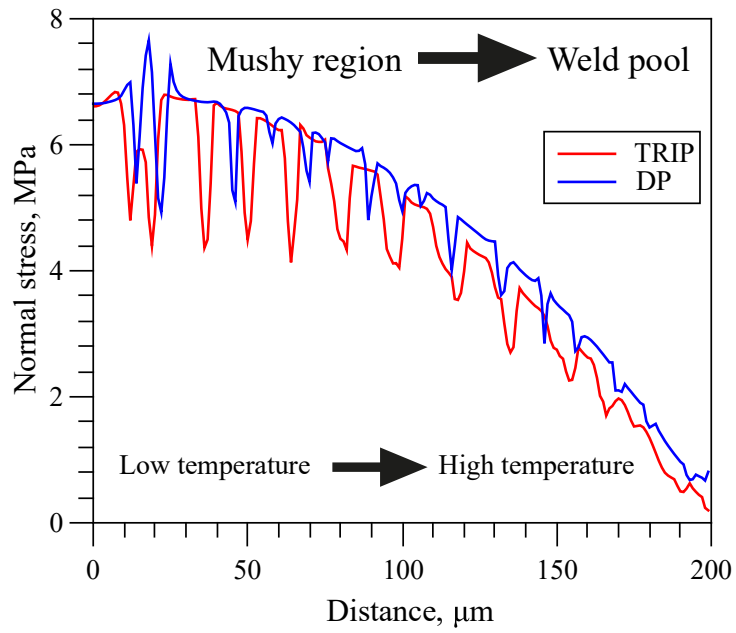


Fig. 9 Normal stress distribution in TRIP and DP steel along the arrow indicated in figure 8 (h).

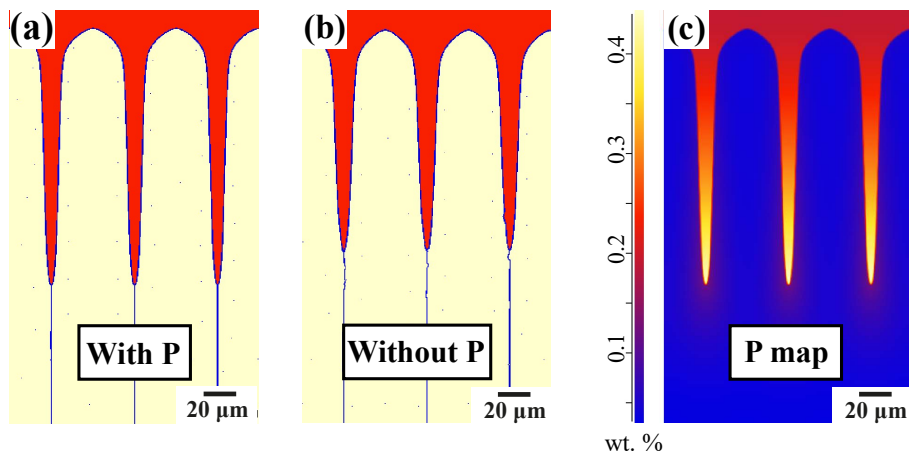


Fig. 10 Phase field simulation showing liquid channel morphology and microsegregation. (a) TRIP steel composition, (b) TRIP-No P steel composition, (c) Phosphorus map in TRIP steel. Adapted from reference [23].

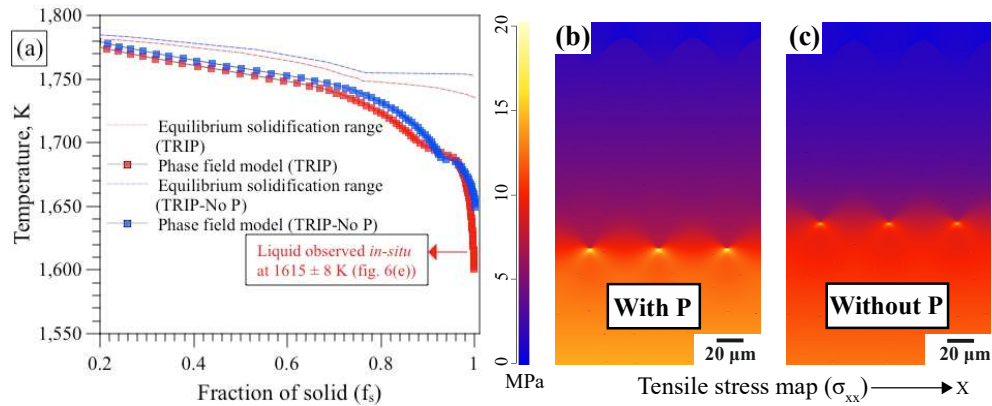


Fig. 11 (a) T vs. f_s curves for the two steels from equilibrium phase diagram and phase field simulations, (b) and (c) tensile stress map in TRIP and TRIP-No P steel respectively. Taken from reference [23].

DISCUSSION

Both the experimental and numerical approaches indicate a higher cracking susceptibility in TRIP steel than in the DP steel. Solidification cracking was not observed in the DP steel. The factors (or combination of factors) that affect cracking susceptibility are discussed below.

SOLIDIFICATION TEMPERATURE RANGE

The equilibrium solidification temperature range of TRIP and DP steel composition is 50 K and 33 K respectively. In general, a wider solidification temperature range leads to a wider mushy region, which in turn increases the susceptibility to cracking [33]. The brittle temperature range (BTR), defined as the temperature range over which a material exhibits loss in ductility is also influenced by the material's solidification temperature range [33–34]. Phosphorus segregation in the TRIP steel leads to undercooling and widens the effective solidification temperature range. Experimental observation of liquid droplets at approximately 1615 K, as shown in figure 7 (e), means that an undercooling of more than 160 K existed during the solidification of the TRIP steel. Note that P in TRIP steel is intentionally added as it helps to retard cementite precipitation, partially replaces Si and provides solid solution strengthening [23]. The P content in DP steel was limited to 30 ppm and isolated liquid droplets at low temperature were not observed during solidification. Temperature *versus* solid fraction curves obtained from phase field simulation, as shown in figure 11 (a) also indicate that the presence of a comparatively large amount of P leads to significant undercooling. In our earlier study [23], atom probe tomography revealed that P content in the interdendritic region is as high as 0.29 wt. %.

INTERDENDRITIC LIQUID FEEDING

Sufficient interdendritic liquid feeding is required to compensate for both the solidification shrinkage and thermal contraction. Darcy's law is often used to describe liquid flow in the mushy region. The law is given as [23]:

$$v_l f_l = -\frac{K \Delta P}{\mu Z} \quad (4)$$

here, v_l is the interdendritic fluid velocity, f_l is the fraction of liquid, K is the permeability of the solid network, μ is the viscosity of the liquid, ΔP is the pressure difference between the dendrite root and tip and Z is the channel length. Here, Z refers to the dendrite growth direction (figure 10). With the same solid fraction (f_s), longer and narrower liquid channels exist in TRIP steel due to the microsegregation of P. Adequate liquid feeding is thus more difficult in TRIP steel than in DP steel. In our recent work, liquid feeding in the interdendritic regions was observed in DP steels [4], whereas, no liquid feeding and solidification cracking were observed in the TRIP steel under similar conditions.

DENDRITIC COHERENCY

At high temperatures within the solidification temperature range, the amount of liquid is high and therefore the solidifying dendrites are surrounded by liquid. From a particular temperature or fraction of solid (dependent on the alloy), a rigid network is formed and the solid structure is able to transmit stresses. The solid network thus becomes coherent. When grain boundaries are involved, the intergranular coalescence temperature is generally low as compared with the intragranular coalescence temperature. This happens when the grain boundary energy (γ_{gb}) is higher than twice the solid-liquid interface energy (γ_{sl}) [36]. From the phase field results, secondary dendritic arms are more prevalent in the TRIP steel than in the DP steel. In addition, a higher P content also increases the secondary dendrite arm spacing. Thus, dendritic coherency in the TRIP steel is reached at a lower temperature compared to the case of DP steel. This is also evident from figures 8(c) and (e). Delayed coherency of the mushy zone in the TRIP steel increases the susceptibility to solidification cracking. The prominent dip in normal stress at the grain boundaries in the TRIP steel (figure 9) further indicates that liquid films tend to persist for a longer time in the TRIP steel. As a result, the solid network is rendered weak and stress is concentrated at the weld centerline, eventually leading to cracking. At the same time, the dendritic network in the DP steel is more coherent and therefore more resistant to cracking.

RESTRAINT

Solidification cracking occurs when the local stress applied to a material is greater than the local strength. Even though TRIP steel is susceptible to solidification cracking, the mechanical restraint is low enough to prevent cracking when welding is carried out beyond a certain distance from the free edge. The reduction in mechanical restraint can therefore

improve the weldability of steels that are otherwise prone to solidification cracking. For example, in our recent work [18], a decrease in heat input led to a decrease in the critical distance beyond which no solidification cracking was observed.

PRESENT WORK IN RELATION WITH EXISTING PHYSICAL MODELS ON HOT CRACKING

A recent criterion of solidification cracking proposed by Kou [9] was applied to both the steels. According to the criterion, the susceptibility of solidification cracking is directly related to the $|dT/d(f_s)^{1/2}|$, near $(f_s)^{1/2} = 1$. Temperature *versus* solid fraction (f_s) curves were obtained using Scheil-Gulliver solidification model. The steepness of the curve (figure 12) in the case of TRIP steel is twice that of DP steel. Therefore, TRIP steel is considered to be more susceptible to cracking.

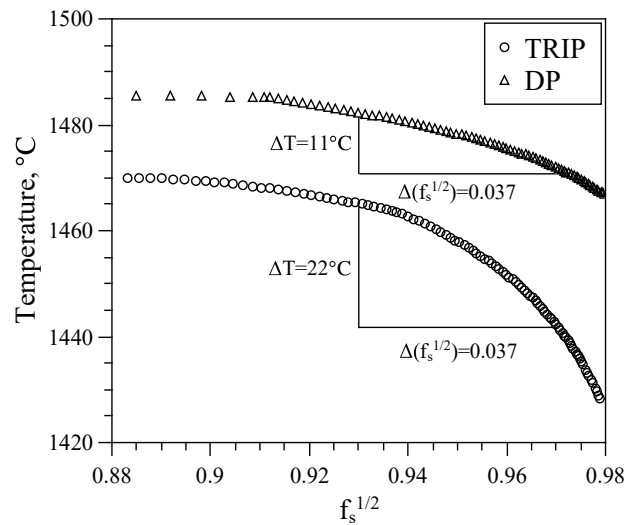


Fig. 12 Prediction of cracking susceptibility using the Kou criterion [9]. Slope of $T - (f_s)^{1/2}$ curves with f_s varying from 0.87 to 0.94 indicates higher crack susceptibility of TRIP steel.

The Rappaz-Drezet-Gremaud criterion [8] was also applied on these steels in our previous work [28]. The liquid pressure drop in the mushy zone is comprised of a pressure drop due to solidification shrinkage together with a thermal deformation term. A larger pressure drop in the liquid increases the susceptibility to cracking. The total pressure drop in the TRIP steel was found to be higher (941.2 kPa) than in the DP steel (10.2 kPa), indicating higher cracking susceptibility in the TRIP steel [28].

Both the criteria are found to be consistent with the cracking susceptibility of the two steels. In general, the applicability of these criteria depends on the accuracy with which the solidification curves can be predicted under welding conditions. Also, it is important to note that all the existing models provide an indication of susceptibility towards solidification cracking. Actual cracking behaviour depends on the welding conditions and in general needs to be determined experimentally. For instance, no solidification cracking was observed in either steel when welding was carried out beyond a certain distance from the

free edge, *i.e.*, restraint effect. The present work was focussed on the (local) governing/contributing factors that affect the solidification cracking susceptibility, using both experimental and modelling approaches. For instance, interdendritic liquid feeding was observed and quantified experimentally [4] and later on studied in relation to solidification cracking susceptibility using phase field solidification models [23], [28]. Solidification models also provided insights into the influence of dendritic coherency and solute segregation on solidification cracking, which is difficult to obtain experimentally.

CONCLUSIONS

A detailed investigation of solidification cracking susceptibility in two common automotive AHSS was carried out by means of both experimental and numerical methods. A novel approach was adopted in which the dynamic thermal conditions behind the moving heat source were extracted from a validated FE-model and applied to a phase field solidification model. Solidification behaviour behind the weld pool was further studied pertaining to the factors, which affect cracking susceptibility. Solidification behaviour during *in-situ* experiments was also studied by means of a phase field model.

The observations from both the laser welding experiments and *in-situ* solidification experiments corroborate the results of phase field modelling. The following conclusions are drawn from the present study:

- The actual solidification temperature range is widened significantly by undercooling in the TRIP steel due to P segregation. A wider solidification temperature range leads to increased susceptibility towards solidification cracking. The solidification rate is faster in the DP steel than in the TRIP steel. In addition, a narrower solidification temperature range in the DP steel entails that the mushy regions spends less time in the crack vulnerable regime.
- Phosphorous microsegregation leads to longer and narrower liquid channels in the TRIP steel. Inadequate liquid feeding thus increases the likelihood of cracking in the TRIP steel.
- In the DP steel, the solid in the mushy region forms a coherent network at an early stage. As a result, it can effectively withstand transverse tensile strains. In the TRIP steel, a continuous network of liquid films persists at the grain boundaries until the latter stages of solidification. As a consequence, tensile strain is concentrated at the weld centreline, eventually leading to cracking.
- Cracking occurs if the threshold strength of a crack susceptible material is exceeded by the mechanical restraint. The amount of restraint affects the local strain and can lead to different cracking behaviour.

In future, solidification models considering interdendritic liquid feeding under welding conditions will be employed. These models will enable further understanding of the solidification cracking phenomena.

ACKNOWLEDGEMENTS

This research was carried out under project numbers F22.8.13485a and F22.8.13485b in the framework of the Partnership Program of the Materials innovation institute M2i (www.m2i.nl) and the Foundation for Fundamental Research on Matter (FOM) (www.fom.nl), which is part of the Netherlands Organisation for Scientific Research (www.nwo.nl). The authors would like to thank the industrial partner in this project 'Tata Steel Nederland B.V.' for the financial support.

REFERENCES

- [1] International Council on Clean Transportation. 'Global passenger vehicle standards (2014)'. Retrieved from <http://theicct.org/info-tools/global-passenger-vehicle-standards>.
- [2] S. KEELER, M. KIMCHI AND P. J. MCONEY: 'Advanced High-Strength Steels Application Guidelines', 2017.
- [3] C. LESCH, N. KWIATON AND F. B. KLOSE: 'Advanced High Strength Steels (AHSS) for Automotive Applications – Tailored Properties by Smart Microstructural Adjustments', *steel research international*, Vol. 88, No. 10, p. 1700210.
- [4] G. AGARWAL, M. AMIRTHALINGAM, S. C. MOON, R. J. DIPPENAAR, I. M. RICHARDSON AND M. J. M. HERMANS: 'Experimental evidence of liquid feeding during solidification of a steel', *Scripta Materialia*, Vol. 146, pp. 105–109, 2018.
- [5] M. RAPPAZ AND J. A. DANTZIG: *Solidification*, 1st ed. EFPL Press, 2009.
- [6] D. G. ESKIN AND L. KATGERMAN: 'A Quest for a New Hot Tearing Criterion', *Metallurgical and Materials Transactions A*, Vol. 38, No. 7, pp. 1511–1519, 2007.
- [7] L. KATGERMAN: 'A Mathematical Model for Hot Cracking of Aluminum Alloys During D.C. Casting', *JOM*, Vol. 34, No. 2, pp. 46–49, 1982.
- [8] M. RAPPAZ, J.-M. DREZET AND M. GREMAUD: 'A new hot-tearing criterion', *Metallurgical and Materials Transactions A: Physical Metallurgy and Materials Science*, Vol. 30, No. 2, pp. 449–455, 1999.
- [9] S. KOU: 'A criterion for cracking during solidification', *Acta Materialia*, Vol. 88, pp. 366–374, 2015.
- [10] N. CONIGLIO AND C. E. CROSS: 'Mechanisms for Solidification Crack Initiation and Growth in Aluminum Welding', *Metallurgical and Materials Transactions A*, Vol. 40, No. 11, pp. 2718–2728, 2009.
- [11] N. CONIGLIO AND C. E. CROSS: 'Initiation and growth mechanisms for weld solidification cracking', *International Materials Reviews*, Vol. 58, No. 7, pp. 375–397, 2013.
- [12] J. K. LARSSON: 'Avoidance of crack inducement when laser welding hot-formed car body components --- a variable analysis', *Physics Procedia*, Vol. 5, pp. 115–124, 2010.
- [13] VDEH: *SEP 1220-3 : Testing and Documentation Guideline for the Joinability of thin sheet of steel - Part 3: Laser beam welding*. 2011.
- [14] M. A. OMAR: 'Automotive Joining', in *The Automotive Body Manufacturing Systems and Processes*, Wiley-Blackwell, 2011, pp. 107–176.
- [15] K.-M. HONG AND Y. C. SHIN: 'Prospects of laser welding technology in the automotive industry: A review', *Journal of Materials Processing Technology*, Vol. 245, pp. 46–69, 2017.
- [16] T. B. HILDITCH, T. DE SOUZA AND P. D. HODGSON: 'Properties and automotive applications of advanced high-strength steels (AHSS)', in *Welding and Joining of Advanced High Strength Steels (AHSS)*, M. Shome and M. Tumuluru, Eds. Woodhead Publishing, 2015, pp. 9–28.
- [17] G. AGARWAL, H. GAO, M. AMIRTHALINGAM AND M. J. M. HERMANS: 'In-situ strain investigation during laser welding using digital image correlation and finite element based

- numerical simulation', *Science and Technology of Welding and Joining*, Vol. 23, No. 2, pp. 134–139, 2018.
- [18] H. GAO, G. AGARWAL, M. AMIRTHALINGAM, M. J. M. HERMANS AND I. M. RICHARDSON: 'Investigation on hot cracking during laser welding by means of experimental and numerical methods', *Welding in the World*, Vol. 62, No. 1, pp. 71–78, 2018.
- [19] A. K. DE, J. G. SPEER AND D. K. MATLOCK: 'Color tint-etching for multiphase steels', *Advanced Materials and Processes*, Vol. 161, No. 2, pp. 27–30, 2003.
- [20] M. REID, D. PHELAN AND R. DIPPENAAR: 'Concentric solidification for high temperature laser scanning confocal microscopy', *ISIJ International*, Vol. 44, No. 3, pp. 565–572, 2004.
- [21] S. GRIESSER AND R. DIPPENAAR: 'Enhanced Concentric Solidification Technique for High-Temperature Laser-Scanning Confocal Microscopy', *ISIJ Int.*, Vol. 54, No. 3, pp. 533–535, 2014.
- [22] S. GRIESSER, R. PIERER, M. REID AND R. DIPPENAAR: 'SolTrack: An automatic video processing software for in situ interface tracking', *Journal of Microscopy*, Vol. 248, No. 1, pp. 42–48, 2012.
- [23] G. AGARWAL, A. KUMAR, H. GAO, M. AMIRTHALINGAM, S. C. MOON, R. J. DIPPENAAR, I. M. RICHARDSON AND M. J. M. HERMANS: 'Study of Solidification Cracking in a Transformation-Induced Plasticity-Aided Steel', *Metallurgical and Materials Transactions A: Physical Metallurgy and Materials Science*, Vol. 49, No. 4, 2018.
- [24] N. SHANMUGAM, G. BUVANASHEKARAN, K. SANKARANARAYANASAMY AND S. R. KUMAR: 'A transient finite element simulation of the temperature and bead profiles of T-joint laser welds', *Materials and Design*, Vol. 31, No. 9, pp. 4528–4542, 2010.
- [25] J. MA, F. KONG AND R. KOVACEVIC: 'Finite-element thermal analysis of laser welding of galvanized high-strength steel in a zero-gap lap joint configuration and its experimental verification', *Materials and Design*, Vol. 36, pp. 348–358, 2012.
- [26] M. ZAIN-UL-ABDEIN, D. NELIAS, J.-F. JULLIEN AND D. DELOISON: 'Prediction of laser beam welding-induced distortions and residual stresses by numerical simulation for aeronautic application', *J. Mater. Process. Technol.*, Vol. 209, No. 6, pp. 2907–2917, 2009.
- [27] Y. PAN: *Laser welding of Zinc coated steel without pre-set gap*, TU Delft, 2011.
- [28] H. GAO, G. AGARWAL, M. AMIRTHALINGAM AND M. J. M. HERMANS: 'Hot cracking investigation during laser welding of high-strength steels with multi-scale modelling approach', *Science and Technology of Welding and Joining*, Vol. 23, No. 4, pp. 287–294, 2018.
- [29] M. AMIRTHALINGAM, E. M. VAN DER AA, C. KWAKERNAAK, M. J. M. HERMANS AND I. M. RICHARDSON: 'Elemental segregation during resistance spot welding of boron containing advanced high strength steels', *Weld. World*, Vol. 59, No. 5, pp. 743–755, 2015.
- [30] W.-Y. WANG, B. LIU AND V. KODUR: 'Effect of temperature on strength and elastic modulus of high-strength steel', *Journal of Materials in Civil Engineering*, Vol. 25, No. 2, pp. 174–182, 2013.
- [31] C. BORDREUIL AND A. NIEL: 'Modelling of hot cracking in welding with a cellular automaton combined with an intergranular fluid flow model', *Computational Materials Science*, Vol. 82, No. Supplement C, pp. 442–450, 2014.
- [32] T. SOYSAL AND S. KOU: 'A simple test for assessing solidification cracking susceptibility and checking validity of susceptibility prediction', *Acta Materialia*, Vol. 143, pp. 181–197, 2018.
- [33] S. KOU: 'Welding Metallurgy', in *Welding Metallurgy*, John Wiley & Sons, Inc., 2003.
- [34] C. E. CROSS: 'On the Origin of Weld Solidification Cracking', in *Hot Cracking Phenomena in Welds*, T. Böllinghaus and H. Herold, Eds. Springer Berlin Heidelberg, 2005, pp. 3–18.
- [35] J. C. LIPPOLD: *Welding Metallurgy and Weldability*. John Wiley & Sons, 2014.
- [36] N. WANG, S. MOKADEM, M. RAPPAZ AND W. KURZ: 'Solidification cracking of superalloy single- and bi-crystals', *Acta Materialia*, Vol. 52, No. 11, pp. 3173–3182, 2004.